Earth and Planetary Science Letters 503 (2018) 1–9

Contents lists available at ScienceDirect

Earth and Planetary Science Letters

www.elsevier.com/locate/epsl

Melting behavior of the lower-mantle ferropericlase across the spin crossover: Implication for the ultra-low velocity zones at the lowermost mantle

Suyu Fu [a], Jing Yang [a], Youjun Zhang [b], Jiachao Liu [a], Eran Greenberg [c], Vitali B. Prakapenka [c], Takuo Okuchi [d], Jung-Fu Lin [a,*]

[a] Department of Geological Sciences, Jackson School of Geosciences, The University of Texas at Austin, Austin, TX78712, USA
[b] Center for High Pressure Science and Technology Advanced Research (HPSTAR), Shanghai 201900, China
[c] Center for Advanced Radiation Sources, University of Chicago, IL, USA
[d] Institute for Planetary Materials, Okayama University, Japan

ARTICLE INFO

Article history:
Received 23 May 2018
Accepted 11 September 2018
Available online 24 September 2018
Editor: B. Buffett

Keywords:
melting behavior
ferropericlase
spin crossover
lower mantle

ABSTRACT

Preferential iron partitioning into melt during melting and crystallization of lower mantle minerals – bridgmanite and ferropericlase – can play a critical role in our understanding of the origin of the early Earth and its evolution to form chemically and seismically distinct regions in the present lowermost mantle. Of particular interest is the consequence of iron spin crossover in ferropericlase on the physical and chemical properties of the molten materials under relevant pressure–temperature (P–T) conditions of the lowermost mantle. However, the spin crossover in liquid (Mg, Fe)O and its effects on melting curves, iron partitioning, melt density – and thus the evolution of an early basal magma ocean – remain poorly studied. Here we conducted high P–T melting experiments on ferropericlase with a starting composition of $(Mg_{0.86}Fe_{0.14})O$ using synchrotron X-ray diffraction up to ~120 GPa and ~5400 K in laser-heated diamond anvil cells, together with chemical analyses on quenched samples using focused ion beam and energy dispersive spectroscopy technique. An ideal solid solution model could be satisfactorily used to fit the experimental data of the liquidus and solidus of (Mg, Fe)O for pure high-spin (HS, below ~83 GPa), and low-spin (LS, above ~120 GPa) states, respectively. The experimental solidus and liquidus at 99 GPa and ~4000–5200 K strongly deviate from ideal solid solution behavior for pure HS and LS states alone, but can be qualitatively explained using a thermodynamics model for a mixture of HS and LS states across the spin crossover. We found that LS (Mg, Fe)O exhibits ~6–8% lower solidus and liquidus temperature than its HS counterpart. Furthermore, our results show that iron preferentially partitions into melt within the spin crossover to generate iron-rich LS melt. Such iron-rich LS (Mg, Fe)O is ~27(±5)% denser than materials expected for lowermost mantle and could potentially persist as residual melt in the lowermost mantle at the late stage of magma ocean crystallization. Modeled results indicate that the existence of the dense, iron-rich LS (Mg, Fe)O melt in the lowermost mantle could provide plausible explanations for characteristic seismological signatures of ultra-low velocity zones (ULVZs).

1. Introduction

Melting phenomena play an important role in the origin of the deep Earth, as well as its evolution and differentiation into the layered structures – metallic core, silicate mantle, and crust (e.g., Walter and Trønnes, 2004). Large-scale collision in the final stage of the planetary formation, such as the Moon-forming giant impact, has been suggested to release huge amount of energy, which can raise the temperature of Earth's interior by thousands of degrees and cause partial or even full melting of the early Earth materials (e.g., Pahlevan and Stevenson, 2007). A global basal magma ocean could also be formed at a later stage of the melting process (Tonks and Melosh, 1993). Geodynamic modeling indicate that the dense iron-rich silicate melt could drop down and be trapped in the lowermost mantle (e.g., Labrosse et al., 2007; McNamara et al., 2010). Further cooling and differentiation of an early basal magma ocean over an extended geological timescale has been used to explain seismic signatures of ultra-low velocity zones (ULVZs) and large low-shear-velocity provinces (LLSVPs) in present low-

* Corresponding author.
E-mail address: afu@jsg.utexas.edu (J.-F. Lin).

https://doi.org/10.1016/j.epsl.2018.09.014
0012-821X/

ermost mantle (e.g., Boukaré et al., 2015; Labrosse et al., 2007; Nomura et al., 2011). Therefore, a thorough understanding of the melting behavior of constituent phases in the deep Earth's interior could help us better understand the observed geochemical and geophysical signatures of the present Earth's lower mantle and constrain the origin and evolution of the Earth.

Of particular interest to the deep-Earth physical and chemical process is the melting behavior of ferropericlase, the second most abundant mineral in the lower mantle, across the electronic spin crossover of iron (Ghosh and Karki, 2016; Holmström and Stixrude, 2016; Lin et al., 2013). The spin crossover in solid ferropericlase has been found to affect a series of properties including elasticity, rheology, and element partitioning (e.g., Irifune et al., 2010; Mao et al., 2011; Wu et al., 2013). About 1–2% density increase has been observed to occur in ferropericlase across the spin crossover (e.g., Mao et al., 2011). It is thus conceivable that the melting behavior as well as iron partitioning of (Mg, Fe)O could be affected by the spin crossover such that denser LS ferrous iron would differentially partition between solid and melt phases upon melting. Recent experimental measurements on the melting behavior of ferropericlase at experimental pressures ranging from 3 GPa to 80 GPa (Deng and Lee, 2017) suggested that a regular solution model is more appropriate to describe the MgO–FeO system rather than an ideal solution model in earlier studies (Du and Lee, 2014; Zhang and Fei, 2008). A significant decrease in melting curve of (Mg, Fe)O with 10%–25% Fe occurs at ~40–50 GPa, which was suggested to coincide with the spin crossover in ferropericlase (Deng and Lee, 2017). Based on experimental and theoretical results on the spin crossover in ferropericlase at high P–T conditions (Lin et al., 2013; Mao et al., 2011; Speziale et al., 2007; Wu et al., 2013), however, the spin crossover in ferropericlase is expected to occur at relatively higher pressures at elevated temperatures due to the positive transition slope (Holmström and Stixrude, 2015; Mao et al., 2011). The reported melting curve anomaly in ferropericlase reported by Deng and Lee (2017) is unlikely to be associated with the spin crossover alone. Further melting experiments at higher P–T covering the whole spin crossover range are thus needed to reveal the nature of the spin crossover across melting in (Mg, Fe)O and to help us understand the role of the spin crossover on the geochemistry of the lowermost mantle and geodynamic processes of the early Earth.

Here we conducted high-pressure burst laser heating experiments with a heating duration of 1–2 s on ferropericlase ($Mg_{0.86}Fe_{0.14}$)O up to ~120 GPa and ~5400 K in laser-heated diamond anvil cells (LHDACs), coupled with *in situ* X-ray diffraction (XRD) measurements. The quenched samples were recovered from the sample chambers and further chemical and texture analyses were conducted using scanning electron microscope and energy dispersive spectrum (SEM-EDS) analyses after focused ion beam (FIB) cutting. The MgO–FeO binary diagram and their liquidus and solidus are derived at high P–T conditions. These results are thermodynamically modeled and then applied to understand the deep-Earth physical and chemical process at the lowermost mantle regions.

2. Experimental details

Polycrystalline ferropericlase ($Mg_{0.86}Fe_{0.14}$)O was synthesized by sintering stoichiometric mixtures of MgO and FeO powder at approximately 1350 K for 12 h under a controlled H_2–CO_2 atmosphere at the Institute for Study of the Earth's Interior, Okayama University at Misasa. Electron microprobe analysis confirmed a homogeneous chemical composition of the sample with 14 at.% Fe, and XRD results showed the sample was in the B1 structure with a lattice parameter $a = 4.2432\ (12)$ Å at ambient conditions. For high P–T melting experiments, the starting ferropericlase powder was slightly pressed into ~10–15 μm thick disks using a pair of 600 μm culet diamonds, and then loaded into respective sample chambers of short symmetric LHDACs with culet sizes between 300 μm flat and 150–300 μm beveled at 8°. 250-μm thick Re gaskets were pre-indented to ~20–24 GPa using the DACs, and holes were drilled in the pre-indented areas as the sample chambers with a diameter of approximately 60% of the culet sizes. The size of the sample disks loaded into DACs were intentionally prepared to be comparable to that of the sample chambers to maximize the number of melting spots and to allow the recovered samples to be securely held within the gasket chambers. Sample disks of ~10–15 μm thick were sandwiched between two dried KCl layers with a thickness of ~5–8 μm each, which were used as the pressure medium, pressure calibrant, and thermal insulator. 30-min evacuations were performed to each sample chamber before the cell was sealed to remove potential residual water moisture.

High P–T melting experiments on ferropericlase were conducted at the 13ID-D station at the GeoSoilEnviroConsortium for Advanced Radiation Sources (GSECARS) of the Advanced Photon Source (APS), Argonne National Laboratory (ANL). The loaded samples in the DACs were compressed to 43 GPa, 66 GPa, 72 GPa, 86 GPa, and 105 GPa, respectively, at 300 K, and were then heated from both sides of each sample for a duration of 1–2 s (herein called burst-hearing) using a double-sided laser heating system (Prakapenka et al., 2008). The focused laser beam has a spot size of ~15 μm. Such burst-heating technique with flat top focused X-ray beams on both sides of the samples minimizes exposure of the heated sample to the laser beams with less than ~50 K temperature gradient within the heated areas (Prakapenka et al., 2008). Based on theoretical estimations on the Fe–Mg inter-diffusion coefficient in solid and liquid (Mg, Fe)O phase (e.g., Yamazaki and Irifune, 2003), local equilibrium for the melt and coexisting solid phases could be achieved within the 1–2 s heating duration. During the laser heating, *in situ* synchrotron XRD spectra were collected using an incident X-ray beam of ~2 μm in diameter and 0.3344 Å in wavelength (Figs. 1 and S1) (Prakapenka et al., 2008). The XRD patterns of the samples were collected by a MAR CCD or Pilatus 1M CdTe detector before, during, and after the laser-heating as well as for quenched samples at ambient conditions. Assuming a gray-body approximation, temperature of the hot spots during the melting was determined by fitting thermal radiation spectra between 670 to 840 nm to a Plank (or Wien) function (Fig. S2). The temperature was averaged over the exposure time as well as averaged from the temperatures of both sides of the heated sample. Taking all aforementioned uncertainties into account, the uncertainty in temperature reported for each melting spot was typically ~200–300 K. Some previous studies suggest that wavelength-dependent absorption/emission of semi-transparent materials such as ferropericlase needs to be taken into account in order to determine the apparent temperature with several hundred kelvin errors during laser heating in single-sided LHDACs experiments (Deng and Lee, 2017). However, the absorption coefficients of ferropericlase used by Deng and Lee (2017) for temperature correction were measured at high pressures and 300 K by Goncharov et al. (2006). The correction factor can significantly vary with Fe content, spin state of iron, pressure and temperature (Goncharov et al., 2010, 2006). Without knowing the reliable absorption coefficients of ferropericlase at high P–T, the temperature corrections used in Deng and Lee (2017) likely causes major uncertainties in their reported melting temperatures of ferropericlase. Furthermore, the use of single-sided laser-heating with large axial temperature gradients and sample geometry (without pressure medium for Mg-rich sample and MgO as pressure medium for Fe-rich samples) by Deng and Lee (2017) can also contribute to significant experimental uncertainties. Considering all these factors and uncertainties, the potential wavelength-dependent emissivity of ferropericlase was not

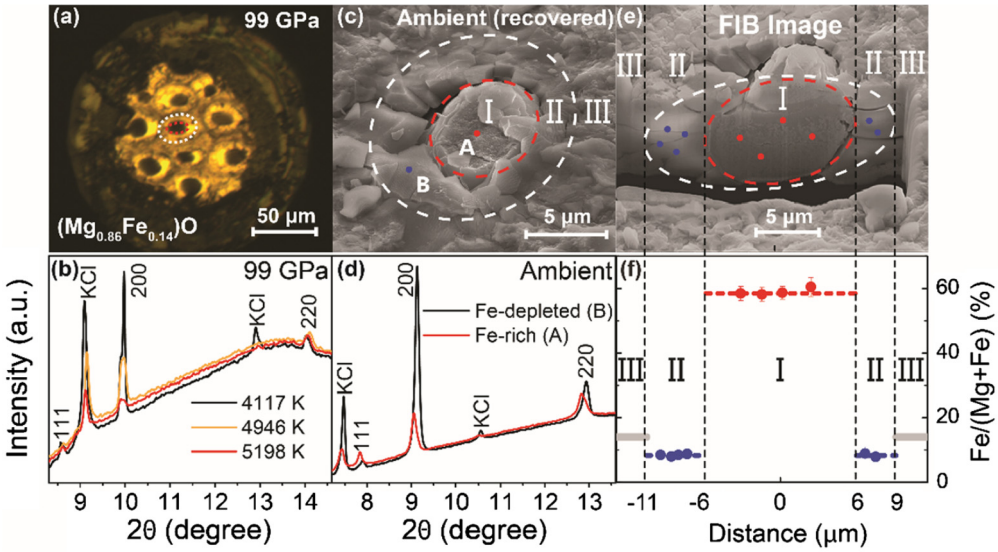

Fig. 1. Melting of ferropericlase $(Mg_{0.86}Fe_{0.14})O$ at ~99 GPa and high temperatures. (a) Optical image of the sample after temperature quenched from laser heating (photo was taken under both transmitted and reflected light). Each darker area in the sample chamber represents a laser-heated spot at a given high temperature, ranging from ~4000 K to ~5400 K (Figs. S1 and S2). (b) *In situ* XRD patterns collected from the heated spots during laser heating. Diffraction peaks of solid ferropericlase are labeled with Miller indices (hkl), and diffraction peaks of B2-structured KCl are labeled as KCl. (c) Laser-heated spot recovered from ~99 GPa and ~4946 K corresponding to areas in dashed circles in (a). (d) XRD patterns at ambient conditions collected from dots A and B of the recovered sample in (c). FIB analyses were conducted on the recovered sample, shown in (e) and (f). (e) Vertical cross section of the laser-heated spot in (c) that was cut using FIB. A significant amount of the quenched sample was removed in FIB cutting to allow reliable analyses without sample blocking EDS signals geometrically. (f) Fe/(Fe+Mg) ratio (%) of the sample in the Regions I and II using EDS analyses. The corresponding positions for the measured spots are marked as small red and blue dots in (e). For comparison, chemical composition for the unheated (fresh) area (Region III) of the sample is shown as horizontal gray lines with 14 at% Fe. (For interpretation of the colors in the figure(s), the reader is referred to the web version of this article.)

considered in our reported temperatures at high pressures. The reported temperature here should be reliable within uncertainty (~200–300 K) (Table S1).

Due to the use of the transparent pressure medium of KCl and its low laser absorption, the pressure determined from its equation of state (EoS) at 300 K (Dewaele et al., 2012) will definitely underestimate the pressure of the hot samples. Here we used two different methods to estimate the thermal pressures at high temperatures (~4000–5400 K). The first approach is to use thermal Birch–Murnaghan EoS to model the experimentally measured P–V–T relations of our ferropericlase sample $(Mg_{0.86}Fe_{0.14})O$ up to 90 GPa and 2100 K. Using the unit cell volume of the heated samples and the thermal EoS, we could calculate the thermal pressures at a given high temperature. To estimate the thermal pressures (ΔP) at higher temperatures where the sample may be melted and could change its composition (and thus cell parameters) due to partitioning, our second approach is to use an empirical correction to count for the isochoric thermal pressures (ΔP_{th}) (Andrault et al., 1998). The ideal isochoric thermal pressures at high temperatures can be expressed as $\Delta P_{th} = \alpha K \Delta T$, where α and K are thermal expansion and bulk modulus, respectively, and ΔT is temperature difference between the heating temperature and the reference temperature (300 K). Due to partial volume relaxation at high temperatures during experiments, studies have indicated that experimental thermal pressures (ΔP) were about half of the ideal isochoric thermal pressures (ΔP_{th}) (Andrault et al., 1998). According to the thermo-elastic parameters of the sample, we have calculated the value of $\Delta P/\Delta T$ as $\sim 3.2 \times 10^{-3}$ GPa/K. Both methods give similar estimations on the thermal pressures of the heated samples within uncertainties. Considering the experimental temperature ranges spanning about 1400 K across melting at 4000–5400 K, the uncertainties of the determined pressures at high temperatures should be approximately one-third of the derived experimental thermal pressures. Therefore, the pressures of 43 GPa, 66 GPa, 72 GPa, 86 GPa, and 105 GPa measured at 300 K in this study, are thermally corrected to be 52(±3) GPa, 77(±3) GPa, 83(±4) GPa, 99(±4) GPa, and 120(±5) GPa, respectively, at high temperatures.

The recovered samples were further analyzed using the FIB system (FEI VERSA 3D type) at the Center for High Pressure Science and Technology Advanced Research (HPSTAR), Shanghai. Heavy gallium ions (Ga^+) were sputtered out from the standards and then accelerated through an electrical field up to 30 kV to produce a field emission focused ion beam. The ion beam currents were set as 30 nA and 10 nA to cut and polish the recovered laser-heated spots, respectively. The FIB system is equipped with a NG Schottky emitter source, which can generate a field emission electron beam for high-quality SEM imaging. Images were taken from the recovered laser-heated spots before and after cutting (Fig. 1). EDS analyses were employed to determine the chemical compositions of the recovered samples in these areas with uncertainties of ~2–5 wt% (Table S1). Knowing that the EDS detector is at 55° from the incident electron beam (Fig. S3), we made sure to remove sufficient materials in the FIB cutting to permit reliable EDS analyses without the EDS signals being blocked off by the sample. We should note that the typical uncertainty of EDS is about 1–2 wt% at 1σ level and uncertainty of wavelength dispersive spectroscopy (WDS) is ~0.1 wt%. Despite the lack of precise measurements using WDS, the composition results of the recovered spots should be reliable within the given uncertainties of ~2–5 wt% (Table S1). These analyses show that Region I is rich in iron compared with the starting sample and the Region I is surrounded by ferropericlase (Region II) that contains less iron than the starting sample (Figs. 1e and 1f). Further SEM-EDS mappings were conducted on the recovered sample (Figs. 2 and S4). The results confirm that the spherical texture is FeO-rich while the surrounding area is MgO-rich. Furthermore, the average content of KCl in these areas is less than 1%, which is almost the uncertainty of EDS technique, indicating that the contamination of KCl in (Mg, Fe)O samples should be negligible. Such small amount of KCl would not be expected to have significant effects on our preliminary results. Previous studies on the dissolution of KCl in MgO indicate that the solubility of MgO in NaCl–KCl melt at 1000 K is very small with a value of K_{sp}(MgO) of $\sim 5.3 \times 10^{-12}$,

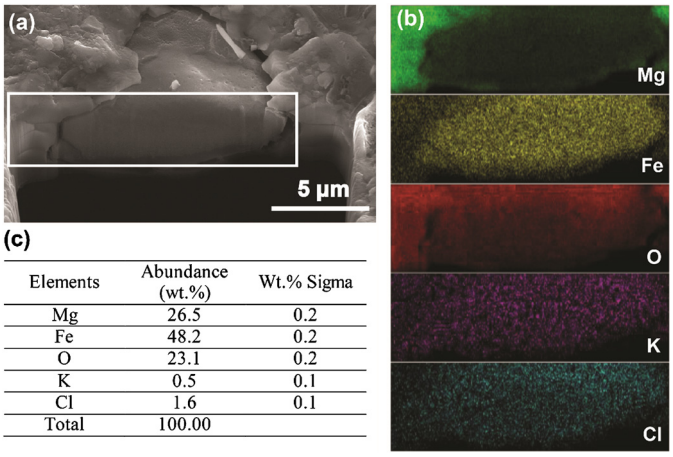

(c)

Elements	Abundance (wt.%)	Wt.% Sigma
Mg	26.5	0.2
Fe	48.2	0.2
O	23.1	0.2
K	0.5	0.1
Cl	1.6	0.1
Total	100.00	

Fig. 2. Representative SEM-EDS mapping of the recovered (Mg, Fe)O sample from ~120 GPa and ~4550 K. (a) Back-scattered electron image of the recovered sample after FIB cutting (the box with white lines shows the area for the mapping analyses in (b); (b) SEM-EDS mapping on the cross section of the recovered sample; (c) chemical analyses for the relative abundance of Mg, Fe, O, K, Cl in the mapped cross section. As shown in (a), we used FIB to remove significant amount of the quenched sample to permit the chemical analysis without samples blocking the EDS signals geometrically. The mapped results indicate that the central region with the spherical texture is iron-rich (Mg, Fe)O and its surrounding is relatively MgO-rich and iron-depleted. The abundance of K and Cl in the recovered sample is low, indicating very limited solubility of KCl thermal insulator in the (Mg, Fe)O sample at high P–T.

less than 0.01 ppb (Combes et al., 1980). This indicates that MgO and KCl are not soluble even in melt phase at high temperatures and only limited amount of KCl could be dissolved into MgO. Considering the 1–2 s heating procedure, the potential melting and contamination of KCl would likely be limited to the contact interface between KCl layers and ferropericlase sample (Fig. S5). As shown in the EDS mapping in Figs. 2 and S4, the cross section of recovered molten spots contains very minimal KCl content.

Several complimentary XRD experiments were conducted to determine the pressure–volume–temperature (P–V–T) relations of the sample. Polycrystalline ferropericlase was mixed with 5 wt% Au as pressure calibrant by mechanically grinding them in a mortar for ~7 h. The mixture was then loaded into the DACs with KCl as pressure medium following the same experimental process reported in a previous study (Mao et al., 2011). XRD patterns of the ferropericlase and Au mixture were then collected up to 90 GPa at 300 K, 1200 K, 1500 K, 1800 K, 2100 K, respectively, in LHDACs to evaluate the thermal EoS parameters of the ferropericlase across the spin crossover (Fig. S6). A complimentary run was also conducted to collect dense data points on the P–V relationship across the spin crossover at room temperature. In this run, we loaded the polycrystalline ferropericlase into sample chambers of symmetric DACs with 200 μm culets. Neon was used as pressure medium and Pt, which was placed in the chamber adjacent to the sample, was used as pressure calibrant. XRD patterns were collected from both the sample and Pt up to 80 GPa at 300 K. We note that the P–V relationship determined using Pt as pressure calibrant and Ne as pressure medium is consistent, within the experimental uncertainty, with the results in the previous run using Au as pressure calibrant and KCl as pressure medium (Fig. S7).

3. Results and data analysis

Fig. 1 shows the representative melting results at ~99 GPa and high temperatures. The central area (Region I, Figs. 1c and 1e) of the laser-heated spots, circled by red dashed lines, shows a brownish color in transmitted light source and a spherical texture, representing the previously molten area. The outer area (Region II) between the white and red dashed lines indicates coexisting solid ferropericlase during the laser-heating induced partial melting. Analyses of the XRD patterns show that the quenched samples in both regions are in the same rock-salt crystal structure but display different lattice parameters (Fig. 1d); the samples in central region have slightly larger d-spacings and consist of iron-rich ferropericlase while the samples in outer region have slightly smaller d-spacings indicative of iron-depleted ferropericlase. Representative SEM-EDS mappings of the recovered spots from high P–T conditions (Figs. 2 and S4) confirm the iron partitioning during the melting of ferropericlase.

Chemical compositions of previously molten and coexisting solid regions were determined using EDS after FIB cutting. These analyses permit us to construct the MgO–FeO binary diagram at high P–T relevant to the lower mantle conditions (Figs. 3, S8 and Table S1). To model the liquidus and solidus of the MgO–FeO binary at high pressures, a thermodynamic model has been developed following the procedure reported in literatures (Wark, 1988). The equilibrium criteria during the melting of ferropericlase can be derived as (see supplementary materials for details):

$$\ln\left[\left(1-X^{S}_{\mathrm{FeO}}\right)/\left(1-X^{L}_{\mathrm{FeO}}\right)\right]=\Delta H^{m}_{\mathrm{MgO}}\left(1/T-1/T^{m}_{\mathrm{MgO}}\right)/R \quad (1)$$

$$\ln\left[\left(1-X^{S}_{\mathrm{MgO}}\right)/\left(1-X^{L}_{\mathrm{MgO}}\right)\right]=\Delta H^{m}_{\mathrm{FeO}}\left(1/T-1/T^{m}_{\mathrm{FeO}}\right)/R \quad (2)$$

where X^{S}_{FeO}, X^{L}_{FeO} are the molar fraction of FeO in solid and liquid phases, respectively; X^{S}_{MgO}, X^{L}_{MgO} are the molar fraction of MgO in solid and liquid phases, respectively; $\Delta H^{m}_{\mathrm{FeO}}$ and $\Delta H^{m}_{\mathrm{MgO}}$ are the enthalpy change of FeO and MgO during the melting process; T^{m}_{FeO} and T^{m}_{MgO} are the melting temperatures of FeO and MgO at a given pressure, respectively; the superscript m denotes melting and R is the gas constant. Remarkable consistency has been reached between experimental data and modeled liquidus and solidus lines at 52 GPa, 77 GPa, 83 GPa and 120 GPa, excepting 99 GPa (detailed modeled parameters are discussed and listed in supplementary materials and Table S2). We note that our data at 52 GPa and high temperatures (thermally corrected from ~43 GPa at 300 K) are consistent with literature reports for the (Mg, Fe)O system at 40 GPa (measured at 300 K) without thermal correction (Du and Lee, 2014). At ~99 GPa, a strong deviation occurs between our experimental data and thermodynamically modeled liquidus and solidus lines of (Mg, Fe)O using the ideal solid solution model. This indicates that the melting of the MgO–FeO binary may become relatively non-ideal due to the occurrence of the LS state at high P–T. Comparison of our results on MgO–FeO phase diagram with that by Deng and Lee (2017) shows significant inconsistency at pressures above 60 GPa (Fig. S9). The major difference is that the liquidus temperature of (Mg, Fe)O by Deng and Lee (2017) is much lower than that observed in this study (Fig. S9). We should note that the pressures reported by Deng and Lee (2017) are measured at 300 K, thus we used the thermal pressure correction methods to correct their pressures at high temperatures for comparison. Such inconsistency likely arises from the use of the temperature corrections by Deng and Lee (2017) without reliable absorption coefficients of ferropericlase with varying Fe content and spin state at high P–T (Goncharov et al., 2010, 2006), as discussed in experimental details.

4. Discussion

4.1. Non-ideal melting of ferropriclase across the spin crossover

To explain the observed non-ideal melting behavior of ferropericlase across the spin crossover, we have determined the pressure–volume–temperature (P–V–T) relations of the ferropericlase based on analyses of collected XRD patterns up to ~90 GPa and ~2100 K

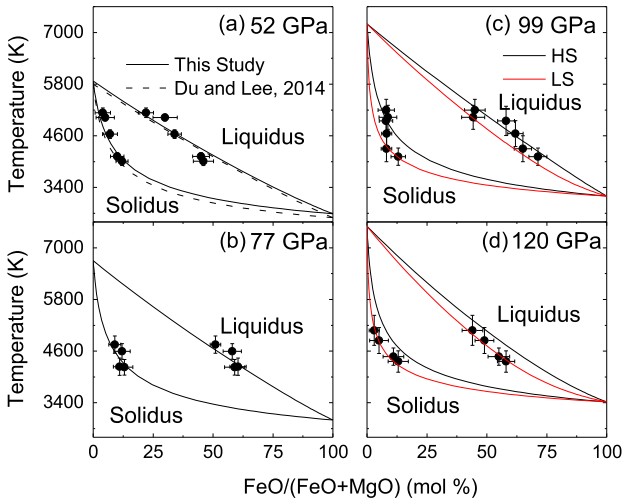

Fig. 3. MgO–FeO binary diagram up to the lowermost mantle pressure. Solid circles: measured compositions for solid and liquid phases; dashed line in (a): literature results for (Mg, Fe)O at pressure ~40 GPa without thermal correction (Du and Lee, 2014). Black and red lines are best fits for HS and LS ferropericlase, respectively, using an ideal solid solution model. The ferropericlase sample remains HS state within the P–T ranges of (a) and (b) (Fig. 4), while LS state occurs at the vicinity of the P–T range in (c), where the experimental data deviates from the ideal solid solution for both HS and LS states. Almost all ferropericlase has transformed to LS state at ~120 GPa and ~4200–5400 K such that the pure LS ideal solid solution model can satisfactorily fit the experimental data in (d).

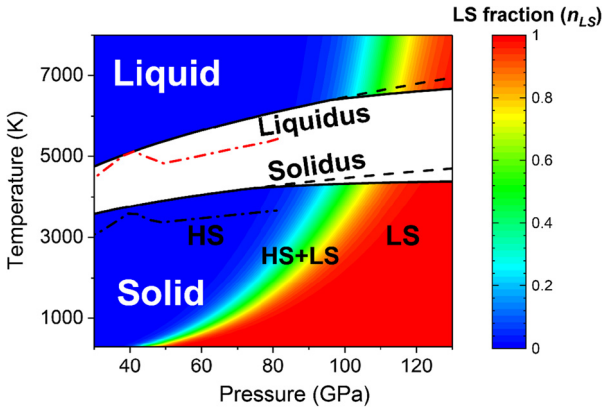

Fig. 4. Spin crossover of iron in ferropericlase ($Mg_{0.86}Fe_{0.14}$)O across solidus and liquidus lines at high P–T relevant to the lower mantle. The solid lines of solidus and liquidus are derived from best fits to experimental data in this study using the Simon–Glatzel equation (Simon and Glatzel, 1929), and the dashed lines are extrapolation from HS state. The spin crossover diagram below the solidus is based on the modeling of experimental XRD data. The phase diagram above the liquidus is derived from melting results and models using the Clausius–Clapeyron equation. According to our thermodynamic modeling, the Clapeyron slope of the spin crossover in liquid (Mg, Fe)O is about two times steeper than that in the solid phases (see supplementary materials for details). The vertical color bar represents the LS fraction (n_{LS}). The dash-dotted lines are solidus and liquidus of ferropericlase with the same composition from a recent literature report (Deng and Lee, 2017).

(Figs. S6 and S7). The derived thermal EoS of solid ferropericlase ($Mg_{0.86}Fe_{0.14}$)O, together with literature results on the spin crossover of ($Mg_{0.75}Fe_{0.25}$)O at high P–T (Mao et al., 2011), allows us to model the P–T dependence of the LS fraction (n_{LS}) for solid ferropericlase (supplementary materials) (Mao et al., 2011). These results are then used to extrapolate the spin crossover diagram to higher pressures (~130 GPa) and temperatures (~4000 K) (Fig. 4). To further evaluate the spin crossover behavior in the liquid ($Mg_{0.86}Fe_{0.14}$)O, one can calculate the P–T dependence of the spin crossover using the Clausius–Clapeyron relation (Wark, 1988):

$$dP/dT = \Delta S/\Delta V \quad (3)$$

where dP/dT is the slope of the tangent to the coexistence curve, ΔV is the specific volume change of the transition, and ΔS is the specific entropy change of the transition. Previous theoretical calculations (e.g., Ghosh and Karki, 2016) and experimental studies (e.g., Mao et al., 2011) have shown that the molar volume of (Mg, Fe)O could decrease about 1–2% across the spin crossover from HS to LS states in both solid and liquid phases; depending on the iron content, the volume decrease can be higher in iron-rich (Mg, Fe)O. To estimate the Clapeyron slope of the spin crossover in liquid (Mg, Fe)O, the entropy change in liquid (Mg, Fe)O from HS to LS states ($\Delta S_{(HS\rightarrow LS)Liq}$) can be derived using the equation:

$$\Delta S_{(HS\rightarrow LS)Liq} = \Delta S_{(HS\rightarrow LS)Sol} + \Delta S_{(Sol\rightarrow Liq)LS} - \Delta S_{(Sol\rightarrow Liq)HS} \quad (4)$$

where $\Delta S_{(HS\rightarrow LS)Sol}$ is the entropy change from HS to LS states in solid ferropericlase; $\Delta S_{(Sol\rightarrow Liq)LS}$ is the entropy change from solid to liquid (Mg, Fe)O for pure LS state; $\Delta S_{(Sol\rightarrow Liq)HS}$ is the entropy change from solid to liquid (Mg, Fe)O for pure HS state. Comparison of the calculated $\Delta S_{(HS\rightarrow LS)Liq}$ and $\Delta S_{(HS\rightarrow LS)Sol}$ suggests that the Clapeyron slope of the spin crossover in liquid ($Mg_{0.86}Fe_{0.14}$)O is still positive and should be about two times steeper than that in the solid phase (supplementary materials and Fig. 4).

Recent theoretical simulations using first-principles molecular dynamics (FPMD) have suggested that the spin crossover pressure in liquid (Mg, Fe)O with a composition of ($Mg_{0.75}Fe_{0.25}$)O is positively correlated with temperature, which almost matches with that in the solid phase (Ghosh and Karki, 2016). However, density-functional theory (DFT) molecular dynamics (MD) computations reported a negative Clapeyron slope of the spin crossover in liquid (Mg, Fe)O with the same composition (Holmström and Stixrude, 2016), in stark contrast with the positive trend in its crystalline phase. The major difference between these studies lies in the calculation of the electronic entropy in liquid (Mg, Fe)O at high temperatures. Generally, the contribution of the spin-dependent entropy in (Mg, Fe)O system can be broken down to $S = S_{mag} + S_{el} + S_{conf}$, where S_{mag} is the magnetic entropy, S_{el} is the electronic entropy due to finite electronic temperature and S_{conf} is the configurational entropy due to interaction between the HS and LS state Fe ions (Holmström and Stixrude, 2016; Wu et al., 2013). The S_{mag} and S_{conf} terms only depend on the Fe content and the LS fraction in the (Mg, Fe)O system (Holmström and Stixrude, 2015; Wu et al., 2013), while the S_{el} term is positively correlated with temperature. As a result, at relatively low temperatures (below the solidus of ferropericlase), the S_{el} term is negligible and the ratio of the HS state increases with increasing temperature due to the dominant contribution from the S_{mag} term to the free energy, which results in a positive Clapeyron slope in solid ferropericlase (Holmström and Stixrude, 2015). Moreover, the contribution of the S_{el} term is amplified at high temperatures and the electronic entropy strongly favors the LS state such that the ratio of the LS state could increase with increasing temperature (a negative Clapeyron slope) in the liquid (Mg, Fe)O when the electronic entropy dominates over the magnetic entropy (Holmström and Stixrude, 2016). Our experimental results and the thermodynamic model allow us to calculate the total entropy change across the spin crossover in liquid (Mg, Fe)O across the P–T range of ~80–120 GPa and ~6000–9000 K. The derived positive Clapeyron slope in liquid (Mg, Fe)O indicates that the S_{el} term is not sufficiently enhanced to dominate over the S_{mag} term in the liquid (Mg, Fe)O system, supporting the reports from Ghosh and Karki (2016). Moreover, the enhanced S_{el} term at high temperatures would contribute to the free energy to some extent, resulting in the Clapeyron slope in liquid (Mg, Fe)O being approximately two times steeper than that in solid phase as shown in this study.

The modeled spin crossover diagram in both solid and liquid (Mg, Fe)O can be used to explain the experimentally observed melting behavior of ferropericlase at high P–T. According to the spin crossover diagram, HS ferropericlase exists up to the P–T conditions of ~83 GPa and ~6000 K such that an ideal solid solution model of the HS ferropericlase can be satisfactorily used to fit our experimental data (Figs. 3 and S8). Non-ideal melting behavior of ferropericlase has been observed with increasing P–T up to ~99 GPa and ~4000–5200 K, which is due to the mixing of HS and LS states. The derived positive Clapeyron slope of the spin crossover in both solid and liquid (Mg, Fe)O phases suggest that the LS fraction would decrease with increasing temperatures at a given pressure (Fig. 4). Consequently, the melting of ferropericlase at ~99 GPa is prone to behave like LS state at relatively low temperatures (~4000 K) with about 80% LS state, while with the temperature up to ~5200 K the solidus line can be better fit for the HS ferropericlase with about 30% LS state (solidus lines in Fig. 3c). We note that the slight mismatch for the liquidus line at ~99 GPa might be additionally associated with compositional effects on the iron-rich side (e.g., Speziale et al., 2007). In addition, almost all ferropericlase transformed to the LS state at 120 GPa and ~4200–5400 K such that an ideal solid solution model for the LS state is sufficient to fit the experimental data (Fig. 3d). These results suggest that the melting behavior of ferropericlase across the spin crossover is non-ideal and depends on the LS fraction in the system. Understanding the influence of P–T and iron content on the spin crossover across the melting in (Mg, Fe)O will require further quantitative experimental and theoretical investigations as well as thermodynamic modeling of the system.

4.2. Melting curves of MgO and FeO endmembers

According to the modeling of the MgO–FeO binary diagram, we derived the melting points of MgO and FeO at high pressures (Fig. 5). These experimental data points for each phase were fitted using the Simon–Glatzel equation (Simon and Glatzel, 1929):

$$T_m = T_0\left(1 + (P_m - P_0)/a\right)^{1/c} \quad (5)$$

where T_m is the melting temperature at a given pressure P_m for MgO and FeO, respectively, a and c are two composition-dependent constants, and T_0 and P_0 are the melting temperature and pressure at the triple point, respectively. The best fits to the data yield $a = 6.98$ (± 1.84) GPa and $c = 3.24$ (± 0.30) with fixed T_0 and P_0 at 3090 K and 0.00001 GPa for MgO (Alfè, 2005; Du and Lee, 2014; Zerr and Boehler, 1994), and $a = 9.58$ (± 1.85) GPa and $c = 3.84$ (± 0.29) with fixed T_0 and P_0 at 1720 K and 0.00001 GPa for FeO (Fischer and Campbell, 2010; Shen et al., 1993), respectively. The melting curve of MgO in this study is consistent with recent DAC experiments at low pressures by Du and Lee (2014) and many theoretical calculations (Alfè, 2005; Boates and Bonev, 2013; Cohen and Weitz, 1998; De Koker and Stixrude, 2009), but much higher than previous data by Zerr and Boehler (1994) and lower than the melting curve from Zhang and Fei (2008). On the other hand, the derived melting curve of FeO in this study has been found to be quite consistent with early experimental investigations using multi-anvil press (Ringwood and Hibberson, 1990) and DACs (Boehler, 1992; Fischer and Campbell, 2010; Shen et al., 1993), excepting some reports with higher melting temperatures (Knittle and Jeanloz, 1991; Zhang and Fei, 2008). The consistency of our results with previous studies on MgO and FeO further affirms the reliability of the derived liquidus and solidus lines of the (Mg, Fe)O at high pressures. Extrapolation of these melting curves to the present CMB pressure suggests that the melting temperatures of MgO and FeO at 135 GPa are about 7800 ± 500 K and 3500 ± 300 K, respectively.

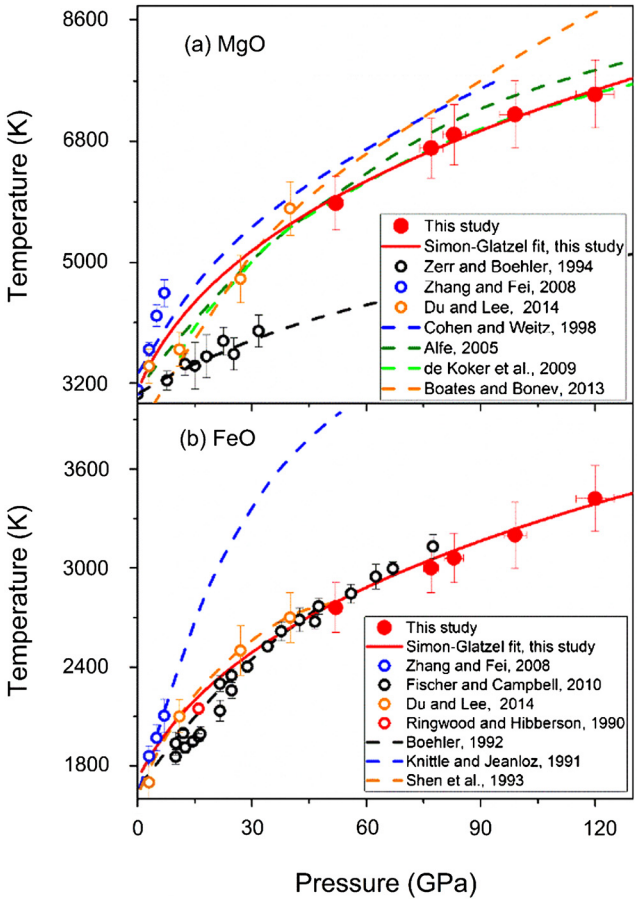

Fig. 5. Melting curves of MgO and FeO endmembers at high pressure. Solid red lines are the best fits to experimental data in this study (solid red circles) using the Simon–Glatzel equation (Simon and Glatzel, 1929). Our data for MgO and FeO are derived from the binary phase diagram shown in Figs. 3 and S8. Open circles in (a): literature experimental results; dashed lines in (a): literature theoretical calculations. Open circles and dashed lines in (b): literature experimental results. Detailed references of these symbols are shown in the legends.

4.3. Iron partitioning during the melting of ferropericlase across the spin crossover

As a solid solution of MgO and FeO, the solidus and liquidus of (Mg, Fe)O would span a wide temperature range between the melting points of the endmember phases at high pressures (Fig. 5). Based on our experimental results, the incorporation of iron into (Mg, Fe)O system would decrease the melting temperature significantly, and the solidus and liquidus temperatures of LS ferropericlase are about 6–8% lower than that of HS state for the same composition (Fig. 4). Moreover, our results show significantly enhanced iron partitioning between solid and liquid (Mg, Fe)O across the spin crossover during the melting of ferropericlase (Fig. 6). Here we consider $(Mg_{0.8}Fe_{0.2})O$, a representative composition of ferropericlase in the pyrolitic model of the present lower mantle (Irifune et al., 2010; Lin et al., 2013), as the composition of the solid phase during the final crystallization process of early Earth. We derived the composition of the coexisting liquid phase and then calculated the iron partition coefficients ($D_{Fe} = X^L_{Fe}/X^S_{Fe}$, where X^L_{Fe} and X^S_{Fe} are the molar fraction of iron content in the liquid and solid phases, respectively) using the modeled MgO–FeO binary diagram at high pressures, together with literature reports (Deng and Lee, 2017; Du and Lee, 2014). Here we observed D_{Fe} is effectively constant at ~3.2 below 70 GPa, while the iron concentration in the liquid across the spin crossover increases by as much as ~12(±3)% compared with that in the HS state. Such enhanced D_{Fe} within the

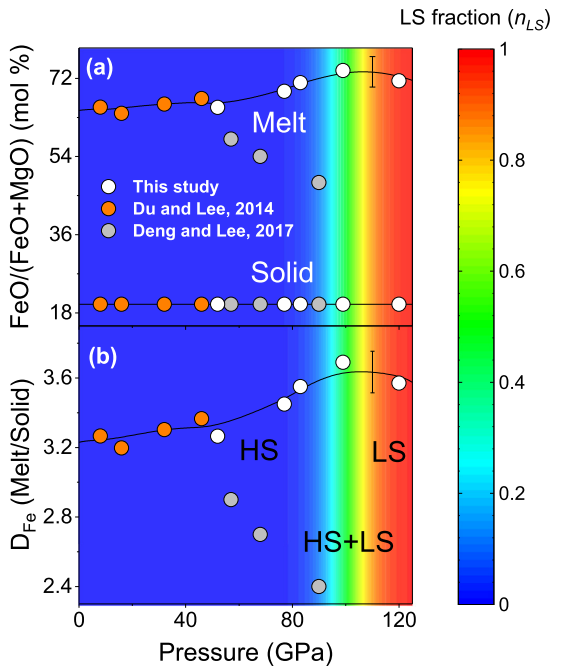

Fig. 6. Iron content in solid and liquid (Mg, Fe)O across the spin crossover at high P–T. (a) Iron concentration in mole percentage in the liquid and solid phases and (b) corresponding iron partition coefficient (D_{Fe}) during the melting of ferropericlase at high pressure. We take $(Mg_{0.8}Fe_{0.2})O$ as the composition of solid phase based on its geochemical relevance in the present Earth's lower mantle to derive the composition of its coexisting liquid phase and D_{Fe} according to the phase diagram in Figs. 3 and S8. Previous results are plotted for comparison, shown as orange circles (Du and Lee, 2014) and gray circles (Deng and Lee, 2017) circles, respectively. The pressures by Deng and Lee (2017) and Du and Lee (2014) are thermally corrected to high temperature conditions using the method discussed in this study. Since our data are, in general, consistent with that by Du and Lee (2014) at relatively lower pressures, the solid lines combining both data sets are plotted to show the high-pressure trend. The black vertical ticks are errors calculated using standard error propagation from the modeled parameters. The color bar on the right shows the modeled LS fractions along the P–T conditions during the melting of ferropericlase, where the coexisting solid phase contains 20 at.% Fe.

spin crossover is associated with the lower solidus and liquidus temperature of the LS state than that of HS state. This is according to our modeled results (Fig. 3), which suggest that the LS Fe would preferentially partition into (Mg, Fe)O melt at a low temperature. Furthermore, the value of D_{Fe} is expected to slightly drop when all Fe has transformed to LS state, at which point the (Mg, Fe)O system behaves as an ideal solid solution similar to that in the HS state. Due to limited data on pure LS state and experimental uncertainty, the difference in D_{Fe} between spin crossover and pure LS regions seems to be small. In comparison, the D_{Fe} decreases from 3.2 to 2.4 at ~80 GPa by Deng and Lee (2017). The significant differences in D_{Fe} between this study and Deng and Lee (2017) at high pressures are due to the inconsistent MgO–FeO phase diagram. The major decrease in D_{Fe} by Deng and Lee (2017) is inconsistent with our current understanding of the melting behavior and the spin crossover of ferropericlase at high P–T (Du and Lee, 2014; Holmström and Stixrude, 2016).

5. Geophysical implications for ULVZs

Ultra-low velocity zones are mapped as thin, localized layers above the core–mantle boundary (CMB) with thicknesses of ~10–30 km, exhibiting a compressional (V_P) and shear (V_S) wave velocity reduction of ~5–20% and ~10–30%, respectively, and an enhanced density of ~5–10% (e.g., Hernlund and Jellinek, 2010; McNamara et al., 2010). Most ULVZs are commonly observed to geographically locate within or near the LLSVPs (Li et al., 2017; McNamara et al., 2010), characterized by lower-than-average V_S velocity (e.g., Garnero et al., 2016). The origin of ULVZs has been thought to be attributable to either the existence of partial melt (Hernlund and Jellinek, 2010; Yuan and Romanowicz, 2017) or local iron-enriched solid heterogeneities (e.g., Liu et al., 2017; Wicks et al., 2017). Geodynamic modeling suggests that the lateral temperature variations in the lowermost mantle might determine the mechanism of the origin of ULVZs; ULVZs located outside or at the edges of LLSVPs are compositionally distinct from their surroundings, while ULVZs located within LLSVPs may be caused by partial melting, where has been suggested to be the potentially hottest regions in the lowermost mantle (Li et al., 2017). Recent tomographic observations of a large ULVZ with an axisymmetric shape near the root of the Iceland hot spot provide seismic evidence for partial melting within the LLSVPs in the lowermost mantle (Yuan and Romanowicz, 2017).

Survival of partial melt in the lowermost mantle would depend on both gravitational and thermodynamic stability. Such partial melt could exist in the deep mantle only if the melt is much denser than the surrounding materials and chemical equilibrium between the melt and solid can be achieved (Boukaré et al., 2015; Labrosse et al., 2007). Considering that ferropericlase is likely the dominant phase hosting Fe below the mid lower-mantle (e.g., Irifune et al., 2010) and that the (Mg, Fe)O melt can accommodate a significant amount of iron during the melting of mantle materials compared to (Al,Fe)-bearing bridgmanite (Nomura et al., 2011), the iron partitioning in solid–liquid (Mg, Fe)O should predominantly control the density contrast between the iron-rich melt and coexisting iron-poor solid during the segregation of an early magma ocean. Our results display a striking increase of D_{Fe} up to a value of ~3.7 for the melting of ferropericlase within the spin crossover, suggesting that the melt would be $(Mg_{0.28}Fe_{0.72})O$ (fp72) with the coexisting solid as $(Mg_{0.8}Fe_{0.2})O$. The calculated density contrast between melt and solid for the pure LS state from literature results (Ghosh and Karki, 2016) shows that the melt is approximately 27(±5)% denser than the coexisting solid under deep mantle conditions (Fig. S12). Geodynamic models have suggested that such dense materials could sink and be trapped near the CMB due to gravitational stability during the initial melting of early Earth (Boukaré et al., 2015; Labrosse et al., 2007; Li et al., 2017). Furthermore, we observed that this fp72 melt has much lower solidus and liquidus temperatures than its HS counterpart, $MgSiO_3$ bridgmanite (Stixrude and Karki, 2005), peridotite (Fiquet et al., 2010), and chondrite (Andrault et al., 2011) due to the effects of iron enrichment as well as spin crossover, as discussed above (Fig. 7). We note that the solidus temperature of fp72 phase is comparable to that of a pyrolitic composition with ~400 p.p.m. water (Nomura et al., 2014). However, the amount of H_2O in the lowermost mantle is still debated. Compared with the estimated thermal structure of the lowermost mantle (Anzellini et al., 2013; Brown and Shankland, 1981), the LS fp72 melt observed here has such a low solidus temperature that it is expected to exist and remain as the last residual melt phase throughout the cooling and crystallization process of the deep magma ocean in the lowermost mantle.

The existence of such dense, LS iron-rich (Mg, Fe)O dominant melt in the lowermost mantle could increase the density and reduce the sound velocities, and therefore match the observed features of the ULVZs. We modeled the V_P, V_S and density of a partially molten lowermost mantle, a mixture between the solid silicate mantle and the liquid $(Mg_{0.28}Fe_{0.72})O$ with certain volume fractions (see supplementary materials for modeled methods and Fig. 8). The modeled results suggest that about 5–20 vol.% residual melt of the partially molten dense (Mg, Fe)O existing near the CMB could explain the seismic observations in the ULVZs, depending on the dihedral angles. We determine that 5–12 vol.% fp72

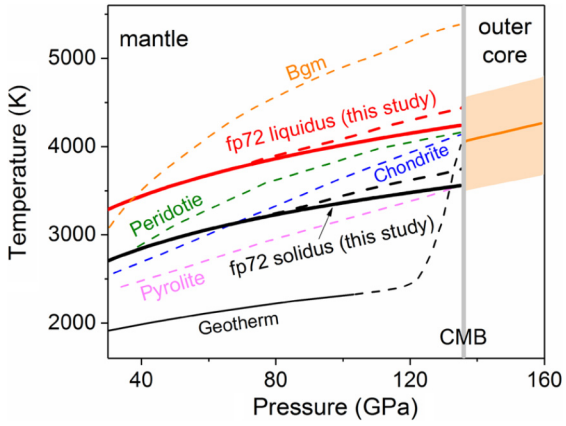

Fig. 7. Melting curves of candidate lower-mantle materials and an expected geotherm of the deep Earth. The melting curves of solidus (solid black) and liquidus (solid red) of $(Mg_{0.28}Fe_{0.72})O$ at high pressure are derived from our experimental results. The dashed red and black lines are the liquidus and solidus of the extrapolated HS state, respectively. These results are compared with previous results on the melting temperature of lower mantle candidate materials including $MgSiO_3$ bridgmanite (Stixrude and Karki, 2005) (dashed orange line), peridotite (Fiquet et al., 2010) (dashed olivine line for solidus), chondrite (Andrault et al., 2011) (dashed blue line for solidus) and pyrolite with ~400 p.p.m. H_2O (Nomura et al., 2014) (dashed magenta line for solidus). The expected geotherm of the lower mantle (Brown and Shankland, 1981) and the outer core (Anzellini et al., 2013) are plotted for comparison. fp72: $(Mg_{0.28}Fe_{0.72})O$. Bgm: $MgSiO_3$ bridgmanite.

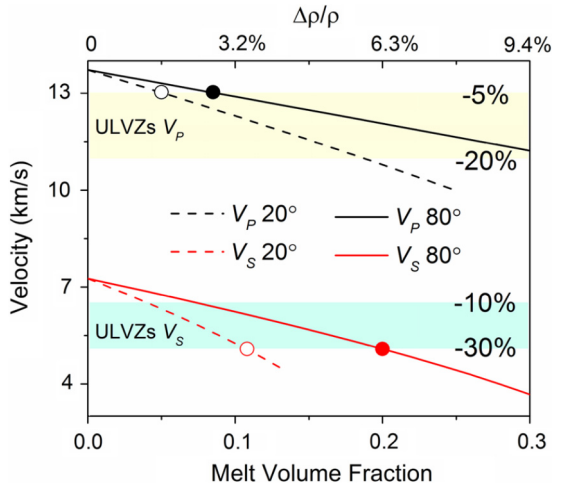

Fig. 8. Compressional (V_P) and shear (V_S) wave velocities of a mixture of solid mantle and residue of partially molten fp72, $(Mg_{0.28}Fe_{0.72})O$, with a given volume fraction at lowermost mantle P–T conditions (see supplementary materials for details). Solid and dashed lines represent different dihedral angles between the partial melt and coexisting solid with values of 20° and 80°, respectively. Yellow and light blue regions represent seismic observed reductions in V_P and V_S at the ULVZs. Density anomalies caused by the fp72 residue melt are shown on the top axis.

melt is needed for a dihedral angle of 20°, whereas 9–20 vol.% melt is required for a dihedral angle of 80°. Early studies on the properties of partial melt in the lowermost mantle suggest that the dihedral angle could determine the properties of the melt, and thus how the ULVZs form and evolve as well as their shape and location (e.g., Liu et al., 2016). For a small dihedral angle, the melt is readily able to wet the grain boundaries, and ultimately merge into the core, whereas the melt with a large dihedral angle would not wet the grain boundaries and could stay trapped in the solid silicate mantle. Such residual melt could potentially accumulate within or near LLSVPs (Li et al., 2017; McNamara et al., 2010), and might be stirred within the ULVZs, which keeps this melt from draining into the core (Hernlund and Jellinek, 2010).

6. Conclusion

In summary, we experimentally constructed temperature-composition ($T-X$) phase diagram of (Mg, Fe)O up to ~120 GPa. An ideal solid solution model could be satisfactorily applied to the melting behavior of both HS and LS ferropericlase, while the LS fraction in the (Mg, Fe)O system could affect its melting behavior and result in a non-ideal melting across the spin crossover. Using the modeled parameters for the liquidus and solidus of (Mg, Fe)O at high P–T, the spin crossover in liquid (Mg, Fe)O was constrained from experiments for the first time. The calculated Clapeyron slope in liquid (Mg, Fe)O is positive and about two times steeper than that in solid phase. The measured $T-X$ phase diagram of (Mg, Fe)O shows that iron preferentially partitions into melt during the melting process, indicating that dense iron-rich (Mg, Fe)O melt was likely to form in the lowermost mantle conditions during the melting of the early Earth. Our observations and modeling in this study suggest that the dense, LS iron-rich (Mg, Fe)O melt is expected to be the most potential phase with essential chemical and physical properties to explain seismological observations and maintain a geodynamical equilibrium at the ULVZs.

Acknowledgements

The authors thank H. Yang for their assistance on the data collection of XRD spectra at 13IDD, GSECARS. We acknowledge D. Huang, Y. Wang and Z.L. Fan for the FIB/EDS analysis, and T. Tomioka for sample synthesis and analyses. The authors also thank R.H. Roberts for language polishing and S. Grand for the constructive suggestions and discussions. J.F.L. acknowledges support from the Geophysics and CSEDI Programs of the U.S. National Science Foundation (NSF), Deep Carbon Observatory (DCO) of the Alfred P. Sloan Foundation, Visiting Professorship of the Okayama University, and Center for High Pressure Science and Technology Advanced Research (HPSTAR). Y.Z. acknowledges support from the National Natural Science Foundation of China (41804082). High $P-T$ melting experiments were conducted at GeoSoilEnviroCARS of APS, ANL. GeoSoilEnviroCARS operations are supported by the National Science Foundation-Earth Sciences (EAR-1128799) and the U.S. Department of Energy, Geosciences (DE-FG02-94ER14466).

Appendix A. Supplementary material

Supplementary material related to this article can be found online at https://doi.org/10.1016/j.epsl.2018.09.014.

References

Alfè, D., 2005. Melting curve of MgO from first-principles simulations. Phys. Rev. Lett. 94, 235701.
Andrault, D., Bolfan-Casanova, N., Nigro, G.L., Bouhifd, M.A., Garbarino, G., Mezouar, M., 2011. Solidus and liquidus profiles of chondritic mantle: implication for melting of the Earth across its history. Earth Planet. Sci. Lett. 304, 251–259.
Andrault, D., Fiquet, G., Itie, J.-P., Richet, P., Gillet, P., Hausermann, D., Hanfland, M., 1998. Thermal pressure in the laser-heated diamond-anvil cell: an X-ray diffraction study. Eur. J. Mineral., Ohne Beihefte 10, 931–940.
Anzellini, S., Dewaele, A., Mezouar, M., Loubeyre, P., Morard, G., 2013. Melting of iron at earth's inner core boundary based on fast X-ray diffraction. Science 340, 464–466.
Boates, B., Bonev, S.A., 2013. Demixing instability in dense molten $MgSiO_3$ and the phase diagram of MgO. Phys. Rev. Lett. 110, 135504.
Boehler, R., 1992. Melting of the Fe–FeO and the Fe–FeS systems at high pressure: constraints on core temperatures. Earth Planet. Sci. Lett. 111, 217–227.
Boukaré, C.E., Ricard, Y., Fiquet, G., 2015. Thermodynamics of the MgO–FeO–SiO_2 system up to 140 GPa: application to the crystallization of Earth's magma ocean. J. Geophys. Res., Solid Earth 120, 6085–6101.
Brown, J., Shankland, T., 1981. Thermodynamic parameters in the Earth as determined from seismic profiles. Geophys. J. Int. 66, 579–596.
Cohen, R.E., Weitz, J., 1998. The melting curve and premelting of MgO. In: Properties of Earth and Planetary Materials at High Pressure and Temperature, pp. 185–196.

Combes, R., De Andrade, F., De Barros, A., Ferreira, H., 1980. Dissociation and solubility variation vspO^{2-} of some alkaline-earth oxides in molten NaCl–KCl (at 1000 k). Electrochim. Acta 25, 371–374.

De Koker, N., Stixrude, L., 2009. Self-consistent thermodynamic description of silicate liquids, with application to shock melting of MgO periclase and $MgSiO_3$ perovskite. Geophys. J. Int. 178, 162–179.

Deng, J., Lee, K.K., 2017. Viscosity jump in the lower mantle inferred from melting curves of ferropericlase. Nat. Commun. 8, 1997.

Dewaele, A., Belonoshko, A.B., Garbarino, G., Occelli, F., Bouvier, P., Hanfland, M., Mezouar, M., 2012. High-pressure–high-temperature equation of state of KCl and KBr. Phys. Rev. B 85, 214105.

Du, Z.X., Lee, K.K.M., 2014. High-pressure melting of MgO from (Mg, Fe)O solid solutions. Geophys. Res. Lett. 41, 8061–8066.

Fiquet, G., Auzende, A., Siebert, J., Corgne, A., Bureau, H., Ozawa, H., Garbarino, G., 2010. Melting of peridotite to 140 gigapascals. Science 329, 1516–1518.

Fischer, R.A., Campbell, A.J., 2010. High-pressure melting of wüstite. Am. Mineral. 95, 1473–1477.

Garnero, E.J., McNamara, A.K., Shim, S.-H., 2016. Continent-sized anomalous zones with low seismic velocity at the base of Earth's mantle. Nat. Geosci. 9, 481–489.

Ghosh, D.B., Karki, B.B., 2016. Solid–liquid density and spin crossovers in (Mg, Fe)O system at deep mantle conditions. Sci. Rep. 6.

Goncharov, A., Struzhkin, V., Montoya, J., Kharlamova, S., Kundargi, R., Siebert, J., Badro, J., Antonangeli, D., Ryerson, F., Mao, W., 2010. Effect of composition, structure, and spin state on the thermal conductivity of the Earth's lower mantle. Phys. Earth Planet. Inter. 180, 148–153.

Goncharov, A.F., Struzhkin, V.V., Jacobsen, S.D., 2006. Reduced radiative conductivity of low-spin (Mg, Fe)O in the lower mantle. Science 312, 1205–1208.

Hernlund, J.W., Jellinek, A.M., 2010. Dynamics and structure of a stirred partially molten ultralow-velocity zone. Earth Planet. Sci. Lett. 296, 1–8.

Holmström, E., Stixrude, L., 2015. Spin crossover in ferropericlase from first-principles molecular dynamics. Phys. Rev. Lett. 114, 117202.

Holmström, E., Stixrude, L., 2016. Spin crossover in liquid (Mg, Fe)O at extreme conditions. Phys. Rev. B 93, 195142.

Irifune, T., Shinmei, T., McCammon, C.A., Miyajima, N., Rubie, D.C., Frost, D.J., 2010. Iron partitioning and density changes of pyrolite in Earth's lower mantle. Science 327, 193–195.

Knittle, E., Jeanloz, R., 1991. The high-pressure phase diagram of $Fe_{0.94}O$: a possible constituent of the Earth's core. J. Geophys. Res., Solid Earth 96, 16169–16180.

Labrosse, S., Hernlund, J., Coltice, N., 2007. A crystallizing dense magma ocean at the base of the Earth's mantle. Nature 450, 866–869.

Li, M., McNamara, A.K., Garnero, E.J., Yu, S., 2017. Compositionally-distinct ultra-low velocity zones on Earth's core–mantle boundary. Nat. Commun. 8.

Lin, J.F., Speziale, S., Mao, Z., Marquardt, H., 2013. Effects of the electronic spin transitions of iron in lower mantle minerals: implications for deep mantle geophysics and geochemistry. Rev. Geophys. 51, 244–275.

Liu, J., Hu, Q., Kim, D.Y., Wu, Z., Wang, W., Xiao, Y., Chow, P., Meng, Y., Prakapenka, V.B., Mao, H.-K., 2017. Hydrogen-bearing iron peroxide and the origin of ultralow-velocity zones. Nature 551, 494.

Liu, J., Li, J., Hrubiak, R., Smith, J.S., 2016. Origins of ultralow velocity zones through slab-derived metallic melt. Proc. Natl. Acad. Sci. USA 113, 5547–5551.

Mao, Z., Lin, J.F., Liu, J., Prakapenka, V.B., 2011. Thermal equation of state of lower-mantle ferropericlase across the spin crossover. Geophys. Res. Lett. 38.

McNamara, A.K., Garnero, E.J., Rost, S., 2010. Tracking deep mantle reservoirs with ultra-low velocity zones. Earth Planet. Sci. Lett. 299, 1–9.

Nomura, R., Hirose, K., Uesugi, K., Ohishi, Y., Tsuchiyama, A., Miyake, A., Ueno, Y., 2014. Low core–mantle boundary temperature inferred from the solidus of pyrolite. Science 343, 522–525.

Nomura, R., Ozawa, H., Tateno, S., Hirose, K., Hernlund, J., Muto, S., Ishii, H., Hiraoka, N., 2011. Spin crossover and iron-rich silicate melt in the Earth's deep mantle. Nature 473, 199–202.

Pahlevan, K., Stevenson, D.J., 2007. Equilibration in the aftermath of the lunar-forming giant impact. Earth Planet. Sci. Lett. 262, 438–449.

Prakapenka, V., Kubo, A., Kuznetsov, A., Laskin, A., Shkurikhin, O., Dera, P., Rivers, M., Sutton, S., 2008. Advanced flat top laser heating system for high pressure research at GSECARS: application to the melting behavior of germanium. High Press. Res. 28, 225–235.

Ringwood, A., Hibberson, W., 1990. The system Fe–FeO revisited. Phys. Chem. Miner. 17, 313–319.

Shen, G., Lazor, P., Saxena, S.K., 1993. Melting of wüstite and iron up to pressures of 600 kbar. Phys. Chem. Miner. 20, 91–96.

Simon, F., Glatzel, G., 1929. Remarks on fusion pressure curve. Z. Anorg. Allg. Chem. 178, 309–316.

Speziale, S., Lee, V., Clark, S., Lin, J., Pasternak, M., Jeanloz, R., 2007. Effects of Fe spin transition on the elasticity of (Mg, Fe)O magnesiowüstites and implications for the seismological properties of the Earth's lower mantle. J. Geophys. Res., Solid Earth 112.

Stixrude, L., Karki, B., 2005. Structure and freezing of $MgSiO_3$ liquid in Earth's lower mantle. Science 310, 297–299.

Tonks, W.B., Melosh, H.J., 1993. Magma ocean formation due to giant impacts. J. Geophys. Res., Planets 98, 5319–5333.

Walter, M.J., Trønnes, R.G., 2004. Early earth differentiation. Earth Planet. Sci. Lett. 225, 253–269.

Wark, K., 1988. Generalized Thermodynamic Relationships – Thermodynamics. McGraw–Hill, Inc., New York, NY.

Wicks, J., Jackson, J.M., Sturhahn, W., Zhang, D., 2017. Sound velocity and density of magnesiowüstites: implications for ultralow-velocity zone topography. Geophys. Res. Lett. 44, 2148–2158.

Wu, Z., Justo, J.F., Wentzcovitch, R.M., 2013. Elastic anomalies in a spin-crossover system: ferropericlase at lower mantle conditions. Phys. Rev. Lett. 110, 228501.

Yamazaki, D., Irifune, T., 2003. Fe–Mg interdiffusion in magnesiowüstite up to 35 GPa. Earth Planet. Sci. Lett. 216, 301–311.

Yuan, K., Romanowicz, B., 2017. Seismic evidence for partial melting at the root of major hot spot plumes. Science 357, 393–397.

Zerr, A., Boehler, R., 1994. Constraints on the melting temperature of the lower mantle from high-pressure experiments on MgO and magnesiowustite. Nature 371, 506–508.

Zhang, L., Fei, Y., 2008. Melting behavior of (Mg, Fe)O solid solutions at high pressure. Geophys. Res. Lett. 35.